

# Simulation of quiet Sun waves in the Ca II infrared triplet

A. Pietarila<sup>1</sup>, H. Socas-Navarro and T. Bogdan

*High Altitude Observatory, National Center for Atmospheric Research<sup>2</sup>, 3080 Center Green, Boulder, CO 80301, USA*

M. Carlsson

*Institute of Theoretical Astrophysics, University of Oslo, P.O.Box 1029 Blindern, N-0315 Oslo, Norway*

R.F. Stein

*Department of Physics and Astronomy, Michigan State University, East Lansing, MI 48824, USA*

## ABSTRACT

The Ca II infrared triplet around 8540 Å is a good candidate for observing chromospheric magnetism. We show results from combining a radiation hydrodynamic simulation with a Stokes synthesis code. The simulation shows interesting time-varying behavior of the Stokes  $V$  profiles as waves propagate through the lines' formation regions. Disappearing and reappearing lobes in the Stokes  $V$  profiles as well as profile asymmetries are closely related to the atmospheric velocity gradients.

*Subject headings:* line: profiles – Sun: atmosphere – Sun: magnetic fields – Sun: chromosphere

## 1. Introduction

New observational data from the SOHO and TRACE spacecraft have revealed a wide array of wave activity in the corona, for example, the discoveries of EIT waves (Thompson

---

<sup>1</sup>Institute of Theoretical Astrophysics, University of Oslo, P.O.Box 1029 Blindern, N-0315 Oslo, Norway

<sup>2</sup>The National Center for Atmospheric Research (NCAR) is sponsored by the National Science Foundation.

et al. 1998), longitudinal standing waves within coronal loops (Kliem et al. 2002; Wang et al. 2002), and compressible waves in polar plumes (Ofman et al. 1997; DeForest & Gurman 1998; Ofman et al. 1999). Aschwanden (2004) and Nakariakov (2003) give extensive reviews of coronal oscillation observations. These observations underscore the link between wave propagation and magnetic fields.

Similar observational studies of the connection between wave processes and magnetic fields in the chromosphere are challenging: there are few suitable spectral lines and they form under complex non-LTE (nLTE) conditions. Consequently there is no straightforward way to extract information, such as atmospheric temperature and pressure, from these observations. The presence of emission self-reversals in the Ca line cores, due to upward-propagating shock-heated plasma, complicates even the simplest Doppler shift analysis and obscures the true oscillatory signal. The magnetic flux in the quiet Sun is very small ( $\approx 3 \text{ Mx cm}^{-2}$  in the internetwork, Lites (2002)), so useful observations need a high signal-to-noise ratio ( $S/N \geq 10^3$ ), which, when combined with the high time cadence required to resolve the wave propagation, imposes stringent demands on the instrumentation.

Acoustic waves generated by the turbulent solar convection become non-linear and develop into shocks as they propagate into the low density of the chromosphere (Carlsson & Stein 1997). Understanding this complex process is important not only from a fundamental point of view, but also because it has been traditionally thought to be an efficient way to transport energy into the upper atmosphere. In 1948 both Biermann and Schwarzschild proposed that shock waves heat the chromosphere, but in recent times, this heating mechanism has been challenged. Carlsson & Stein (1995) have argued, based on radiation hydrodynamic simulations, as to whether acoustic shocks are capable of heating the non-magnetic chromosphere. And recently Fossum & Carlsson (2005) showed, by comparing radiation hydrodynamic simulations and TRACE observations, that the integrated acoustic wave power, including frequencies up to 50 mHz, is insufficient to heat the non-magnetic chromosphere.

Even if wave propagation is not the sole answer to the heating problem it is still of interest. Atmospheric dynamics depend on wave propagation properties such as wave generation, refraction, reflection, mode coupling and dissipation. Because the three MHD waves, i.e. Alfvén, slow MHD and fast MHD waves, have quite different properties, a lot of information about the atmospheric conditions are embedded in them. In the mid-chromosphere magnetic fields spread out and fill the space, making the term non-magnetic chromosphere applicable at best only in the low quiet Sun chromosphere. The layer where the transition from pressure to magnetic dominated regimes occurs is often referred to as the “magnetic canopy.” Study of TRACE observations has shown that there is more oscillatory power below the canopy than above it (McIntosh et al. 2003) and MHD simulations of wave propagation

have identified this layer as a place where dramatic changes in wave propagation take place (Bogdan et al. 2003). Waves are also used as a tool in “coronal seismology” to probe the physical conditions in the corona. Coronal parameters, e.g. magnetic field strengths and transport coefficients, can be determined by combining measurements of the wave properties and oscillations with theoretical models.

Modeling wave propagation in the solar atmosphere is a daunting task. A realistic model must be three-dimensional (3D). The treatment of radiation should be non-gray and nLTE. The significance of magnetic fields in wave propagation make them an essential part of any comprehensive model. Yet another crucial part of any model describing wave propagation in the chromosphere is nonlinear effects such as wave steepening and shocks. Because of the complexity of the problem, and the computational power needed to solve it, so far no fully comprehensive model has been developed. Instead restricted combinations of the above-mentioned elements have been studied. For example Carlsson & Stein’s (1992, 1994, 1995, 1997, 2002) 1D model combines the nonlinear hydrodynamics with full treatment of radiative transfer. The effect of shock dissipation in the chromosphere has been studied also by e.g. Fawzy et al. (2002), Rammacher & Cuntz (2003), Buchholz et al. (1998), and Skartlien et al. (2000). Bogdan et al. (2003) have looked at the nonlinear non-radiative 2D magnetic problem. Other numerical simulations on MHD wave propagation include e.g.: Ziegler & Ulmschneider (1997), Cargill et al. (1997), Tirry & Berghmans (1997), Huang et al. (1999), McKenzie & Axford (2000), De Groof & Goossens (2000), De Groof et al. (2002), Tsiklauri et al. (2003), Arregui et al. (2003), and Ofman et al. (2000). In this paper we approach the problem from a different perspective.

We have combined full treatment of radiative transfer in 1D with magnetohydrodynamics in 2D. The treatment of the interplay between the hydrodynamics and the magnetic field is effected in a suggestive, although not entirely rigorous fashion. A 1D radiation hydrodynamic simulation (duration of 3690 s) is employed as the base building block. It is used to kinematically deform a 2D initial magnetic field,  $\mathbf{B}_0(x,z)$ , according to the magnetic induction equation,

$$\frac{\partial \mathbf{B}}{\partial t} = \nabla \times [\mathbf{v}(z,t) \times \mathbf{B}(x,z,t)], \quad (1)$$

where  $\mathbf{B}(x,z,t=0) = \mathbf{B}_0(x,z)$  is prescribed and  $\mathbf{v}(z,t) = w(z,t)\mathbf{e}_z$  is derived from the radiation hydrodynamic simulation. By having the plasma- $\beta$ , i.e. the ratio between the gas and magnetic pressures, significantly larger than one, we can justify neglect of the back reaction of the Lorentz force on the dynamics. Finally we integrate the Stokes transfer equation to determine the emergent Stokes profiles in I and V for the Ca II infrared (IR) triplet lines for

each 10 second time step. In this way, all 3 essential ingredients are accounted for in this approach although not fully consistently.

The Ca II infrared triplet is an excellent diagnostic of chromospheric oscillations in sunspots (e.g. Tziotziou et al. 2002; Socas-Navarro et al. 2001; Beckers & Schultz 1972)) and shows promise to be as useful in the quiet Sun. Unfortunately, these lines are usually out of the accessible wavelength range for most modern spectro-polarimetric instrumentation. Currently the newly commissioned Spectro-Polarimeter for INfrared and Optical Regions (SPINOR, Socas-Navarro et al. 2005) and the French-Italian solar telescope THEMIS operated in the MTR-mode (Mein & Rayrole 1985; Rayrole & Mein 1993) can routinely provide high-sensitivity observations of these lines.

The outline of the paper is as follows. In the second section the numerical simulation and initial conditions are described. Then in the third section we show the Stokes profiles produced in the simulation and try to explain how they are formed in terms of the atmospheric dynamics. We find interesting time-dependent behavior in the Stokes V profiles as shocks propagate through the model atmosphere. Disappearing and reappearing Stokes V lobes as well as profile asymmetries are closely related to both the local fluid velocity and atmospheric velocity gradients. Finally, in the fourth section the results are discussed.

## 2. The numerical simulation

Since solving the full 3D nonlinear problem is out of our reach we chose a simplified approach with the main premise being that the magnetic field is weak. This way we could construct a 2D dynamic magnetized atmosphere without needing to take into account the full coupling of the hydrodynamics and the magnetic field. Instead the time evolution of the magnetic field is dictated entirely by the hydrodynamics.

In expanding a 1D hydrodynamic simulation into 2D we made three assumptions. The first one is that the piston used to drive the atmosphere is homogeneous over a larger area. In MDI observations the size of coherently oscillating patches is typically up to 6 Mm in diameter (Judge et al. 2001). Secondly, that there is no horizontal radiative transfer or interference between points. SUMER observations of the UV continua show a sharp contrast between the network and internetwork. This suggests that the length scale of lateral radiative transfer is not large i.e. it is smaller than the SUMER spatial resolution of 1 arc second. Previous simulations by Carlsson and Stein using the radiation hydrodynamic code successfully reproduce observations of the low chromosphere, up to about 1.2 Mm. This implies that the code, even though 1D, captures most essential physical ingredients of the

lower solar atmosphere. And the third assumption is that the filling factor for the magnetic field is 1, i.e. we are fully resolving it.

In the following subsections the three building blocks of the simulation, i.e. the radiation hydrodynamic simulation, adding the magnetohydrodynamics and synthesizing Stokes profiles, will be discussed separately.

## 2.1. Radiation hydrodynamic simulation

We used Carlsson and Stein’s (1992, 1995, 1997, 2002) radiation hydrodynamic code as the starting point for the numerical simulation. Not only did Carlsson and Stein succeed in reproducing the appearance of the Ca II H and K lines, but they also showed beyond doubt the dynamic nature of the solar atmosphere. Their code, which is 1D, non-magnetic, and driven by a piston derived empirically from suitable time series observations, compares with observations of the Ca II H and K bright grains remarkably well, even down to the level of individual grains. They also showed that statistical equilibrium is not a valid approximation for the calculation of hydrogen populations in a dynamic atmosphere. Furthermore, they demonstrated that there is fundamental difference between the static, semi-empirical chromospheric models and a truly dynamic chromosphere.

The radiation hydrodynamic code solves simultaneously the mass, momentum and energy conservation equations and the nLTE radiative transfer equations on an adaptive grid. An adaptive grid allows for higher numerical resolution in regions where it is needed, i.e. shocks, and a coarser discretization in places where a lower resolution is sufficient. Not all species contribute significantly to the thermodynamics, only H, He, and Ca are included in the full-scale radiation hydrodynamic treatment. All continua besides H, Ca, and He are treated as background continua in LTE using the Uppsala opacities code (Gustafsson 1973).

A piston (fluid velocity as a function of time) based on MDI observations is located at the lower boundary and is used to force the atmosphere. Initially the atmosphere (figure 1) is in radiative equilibrium. The radiation field at the lower boundary is optically thick at all wavelengths while the upper boundary is transmitting and is set to have a  $10^6$  K temperature at a fixed height of 10 Mm above the photosphere. In our simulation we used only the first 3.5 Mm since above that the Ca II IR triplet line opacities are small and the region does not contribute to line formation. The coronal irradiation of the chromosphere is based on Tobiska’s formalism (Wahlstrom & Carlsson 1994). For a more detailed discussion of the lower boundary, see Judge et al. (2003).

Figure 2 shows the piston velocity used in the simulation as a function of time. Negative

velocities correspond to an upward movement of the atmosphere. The main frequencies of the driving piston are centered around 3 mHz, i.e. frequency range for p-mode oscillations, which usually dominate the MDI velocity power spectra. There is a slight temporal asymmetry in the piston, with positive velocities being dominant in the first half of the time series. This causes a slow downward movement of the whole atmosphere during the first half of the simulation. This effect can be seen as a slow drift of the column mass at a given height as a function of time (figure 2).

As the density in the atmosphere decreases with height, the velocity amplitudes of waves must increase as they propagate upward in order to approximately conserve the wave energy flux. Eventually, by the mid-chromosphere, the waves steepen and form shocks (figure 3). As the large amplitude waves propagate they push the less dense material in front of them upward compressing and thus heating it. After the shock has passed the material cools and falls down again. This motion is clearly seen in figure 3 where the location of a fixed column mass oscillates as the waves pass by. This oscillatory behavior is manifested dramatically by the periodical change in the location of the large atmospheric temperature gradient, i.e. the transition region. This variation can be up to 0.5 Mm in extent. Most of the heat dissipated from the shock goes into thermal energy instead of ionization because the dynamic timescales are much shorter than the hydrogen ionization/recombination timescales. Hydrogen is by far the most abundant element and therefore very important for the thermodynamics. Ionization does not take place until sometime after the shock front has passed. If LTE was assumed the ionization/recombination would be instantaneous leading to a smaller temperature variation in the shock as shown by Carlsson & Stein (1992).

## 2.2. Magnetohydrodynamical part of the numerical simulation

The time evolution of the magnetic field is governed by the induction equation. Expanding the crossproduct in equation (1) gives:

$$\frac{\partial \mathbf{B}}{\partial t} + (\mathbf{v} \cdot \nabla) \mathbf{B} + \mathbf{B} (\nabla \cdot \mathbf{v}) = (\mathbf{B} \cdot \nabla) \mathbf{v}, \quad (2)$$

where  $\mathbf{v} = w(z,t)\hat{\mathbf{e}}_z$ . The  $z$ -component of equation (2) in a 2D vertically stratified atmosphere is:

$$\frac{\partial B_z}{\partial t} + w \frac{\partial B_z}{\partial z} = \frac{dB_z}{dt} = 0 \quad (3)$$

i.e. the Lagrangian derivative vanishes, but the Eulerian does not. The  $x$ -component of equation (2) is:

$$\frac{\partial B_x}{\partial t} + v_z \frac{\partial B_x}{\partial z} + B_x \frac{v_z}{\partial z} = 0. \quad (4)$$

Dividing by  $\rho$ , and then from this subtracting the equation for conservations of mass,

$$\frac{\partial \rho}{\partial t} + w \frac{\partial \rho}{\partial z} + \rho \frac{\partial w}{\partial z} \cdot \mathbf{v} = 0 \quad (5)$$

multiplied by  $B_x/\rho^2$  gives:

$$\frac{d B_x}{dt \rho} = 0 \quad (6)$$

i.e. it is the Lagrangian derivative of  $B_x/\rho$  that vanishes. The  $B_x$  carried by a given fluid element evolves in the same manner as the density:

$$\frac{B_x(z', 0)}{B_x(z, t)} = \frac{\rho(z', 0)}{\rho(z, t)}, \quad (7)$$

where  $z'$  is the location of the fluid parcel at  $t = 0$  and  $z$  is the position of that same fluid parcel at a later time  $t$ . The density and velocity fields are furnished by the radiation hydrodynamic simulation. With this information, and equations (3) and (6) we can solve for the time evolution of the magnetic field. By doing this we have a 2D magnetized dynamic atmosphere where the hydrodynamics vary only in the vertical direction.

The choice of initial magnetic field is arbitrary as long as the main criterion is fulfilled: the field has to be sufficiently weak. We chose to start out with a potential field. It was constructed from the first 20 coefficients of the Fourier series of a step function and set to decay exponentially with height:

$$\left. \begin{array}{l} B_x(x,z,t=0) \\ B_z(x,z,t=0) \end{array} \right\} = \frac{2B_0}{\pi} \sum_{k=0}^{20} \frac{e^{-\frac{\pi(2k+1)}{H}z}}{2k+1} \left\{ \begin{array}{l} \sin \left[ \frac{\pi(2k+1)}{H} \times x \right] \\ \cos \left[ \frac{\pi(2k+1)}{H} \times x \right] \end{array} \right\}, \quad (8)$$

where  $B_0=150$  G and  $H=0.85$  Mm. The simulation domain spans 0.85 Mm in the horizontal direction with 23 equidistant grid points and about 3.5 Mm in the vertical direction

with 130 adaptive grid points. Note that 3.5 Mm is well above the formation height of the Ca lines.

The magnetic field configuration is quite simple (figure 1). It contains one arcade-like feature that extends from one edge of the domain to the other edge. Near the lower boundary the field strength is 100-250 G, and is largest at the sides of the domain where the field is nearly vertical. In the middle the field is horizontal. The field decays rapidly with height: by 1 Mm the field strength has reduced by roughly two orders of magnitude. The variation of the magnetic pressure in the horizontal direction is by then smoothed out, because the  $k = 0$  term dominates in equation (8) at great heights. Because the initial field is potential, the magnetic field scale height is set by the width of the magnetic loop structure, 0.85 Mm. The plasma- $\beta$  decreases with height in the lower part of the simulation domain (the smallest value in the initial atmosphere is roughly 40), but above 1.2 Mm it begins to increase again. In the lower part, the gas pressure scale height is smaller than the magnetic field scale height. So, the gas pressure drops off faster than the field strength resulting in a decreasing plasma- $\beta$ . However, at about 1.2 Mm the magnetic field scale height becomes smaller than the density scale height, which, unlike the magnetic field scale height, is not constant throughout the atmosphere. This causes the plasma- $\beta$  to increase with height.

As the waves propagate through the atmosphere the magnetic field is rarefied and compressed, and no longer potential. The smallest value of plasma- $\beta$ , 3, occurs at  $\approx 800$  s while the atmosphere is still adjusting to the initial conditions. After this the plasma- $\beta$  is in general over 10 except when large shocks pass by and it decreases to 5-10. Keeping the plasma- $\beta$  large justifies the neglect of the Lorentz force.

### 2.3. Synthesizing the Ca IR triplet Stokes profiles

The nLTE radiative transfer equation is both non-linear (the atomic populations through the radiative transfer equation depend nonlinearly on themselves) and non-local (the radiation field at a given point depends on the radiative processes in the entire atmosphere). Additional challenge rises from the coupling of radiative transitions, i.e. a change in the rate of one radiative transition has an effect on all radiative transitions.

In the polarized case the radiative transfer equation takes the following form (Wittmann 1974):



$$\begin{aligned}
 & \frac{d}{ds} \begin{pmatrix} I \\ Q \\ U \\ V \end{pmatrix} \\
 = & \begin{pmatrix} \epsilon_I \\ \epsilon_Q \\ \epsilon_U \\ \epsilon_V \end{pmatrix} - \begin{pmatrix} \eta_I & \eta_Q & \eta_U & \eta_V \\ \eta_Q & \eta_I & \rho_V & -\rho_U \\ \eta_U & -\rho_V & \eta_I & \rho_Q \\ \eta_V & \rho_U & -\rho_Q & \eta_I \end{pmatrix} \begin{pmatrix} I \\ Q \\ U \\ V \end{pmatrix}
 \end{aligned} \tag{9}$$

or in compact notation:

$$\frac{d\mathbf{I}}{ds} = \mathbf{e} - \mathbf{K}\mathbf{I}, \tag{10}$$

where  $\mathbf{e}$  is the emission vector that accounts for the contributions of spontaneous emission to the intensity and polarization. The propagation matrix is  $\mathbf{K}$ . Its diagonal elements,  $\eta_I$ , are the absorption terms. The dichroic terms,  $\eta_Q$ ,  $\eta_U$  and  $\eta_V$ , relate the intensity with the polarized states, and the dispersion terms,  $\rho_Q$ ,  $\rho_U$  and  $\rho_V$ , couple the different polarized states. These seven independent coefficients are functions of the frequency and other parameters determined by the physical state of the atmosphere, such as the angles defining the direction of the magnetic field.

We used a nLTE Stokes synthesis and inversion code (Socas-Navarro et al. 2000) to synthesize the Ca IR triplet line profiles for the 2D dynamic atmosphere. The code assumes statistical equilibrium and complete redistribution. The atmosphere is dominated by strong UV lines and continua while the lines with large Zeeman splitting are relatively weak and thus cannot produce significant changes in level populations. This justifies the use of the field-free approximation (Rees 1969), i.e. that the magnetic field has no effect on atomic level populations, instead the magnetic sublevels are proportionally populated according to their degeneracy. This reduces the unknowns in the transfer equation to the same unknowns as in the unpolarized case. Atomic polarization can have an effect on the emergent Stokes Q and U profiles, especially in the weak field regime (Manso Sainz & Trujillo Bueno 2003). Because of this we have chosen to consider only Stokes I and V in what follows.

In practice, the code first solves the non-magnetic equation by using the short characteristics method (Kunasz & Auer 1988). Then the formal solution is used to compute the emergent Stokes profiles. The end product is a 2-D time series with the four Stokes parameters for the Ca IR triplet lines and a photospheric Fe I line at 8497 Å blended with the wing

of the 8498 Å line. We do not discuss the Fe I line, instead we focus on the more dynamic Ca lines. Table 1 shows the atomic level configurations and energies for the transitions. Shown in the table are also the heights where the Ca line core optical depths equal unity in the initial simulation atmosphere as well as the minimum, maximum, and mean heights during the entire simulation.

### 3. Results from the numerical simulation

Asymmetries in line profiles are caused by atmospheric gradients in velocity and magnetic field vector. A velocity gradient is always required for an asymmetry. The line absorption profile at a given height is centered around a wavelength given by the Doppler shift of the local fluid velocity. Negative velocities above the main line formation height shift the absorption profile to the blue, causing more absorption and an increase in optical depth at the blue wavelengths while there is less absorption and a smaller optical depth in the red wing. The opposite is true for positive velocity gradients. The shift ultimately results in asymmetries visible in Stokes  $I$ ,  $Q$ ,  $U$ , and  $V$ . Intensity asymmetries due to propagating waves have been discussed in detail for the Ca H and K lines by Carlsson and Stein (1997). Large Stokes  $V$  area asymmetries are the product of both velocity and magnetic field vector gradients while a velocity gradient alone can produce a large amplitude asymmetry (Sanchez Almeida & Lites 1992; Landolfi & Landi degl’Innocenti 1996). In our simulations, because the magnetic field is weak, the velocity gradients have a larger influence than the magnetic field gradients on the formation of the asymmetries. As a result the differences in the shapes of Stokes  $V$  profiles along the horizontal direction are small.

The area asymmetry of a Stokes  $V$  profile can be defined as (Martínez Pillet et al. 1997):

$$\sigma A = s \frac{\int_{\lambda_0}^{\lambda_1} V(\lambda) d\lambda}{\int_{\lambda_0}^{\lambda_1} |V(\lambda)| d\lambda},$$

where  $s$  is the sign of the blue lobe. Because all three lines have a considerable amount of signal in the wings of the Stokes  $V$  profiles, determining the integration range is not trivial. We do not integrate the line profile over the full wavelength range, since that can not be done with real observations. Instead, we chose to determine the wavelength range from the line intensity profiles by stepping toward the red starting from the line core until the intensity is equal to the intensity of the blue wing at 600 mÅ from the core. This ensures that the integration range is centered around the line core, but at the same time a significant amount of signal in the line wings is included in the integration range. The signal in the wings,

especially in the 8498 Å line, has usually very little asymmetry and can overshadow the line core signal making the computed asymmetries smaller than what they would be if only the line core was considered.

The amplitude asymmetry is given by (Martínez Pillet et al. 1997):

$$\sigma a = \frac{a_b - a_r}{a_b + a_r},$$

where  $a_b$  and  $a_r$  are the unsigned extrema of the blue and red lobes of the Stokes  $V$  profile.

### 3.1. Stokes profiles in the initial atmosphere

Since there are no velocity gradients in the initial atmosphere, the Stokes  $I$  and  $V$  profiles for the Ca IR triplet lines are symmetric (figure 4) in the beginning of the simulation. The 8498 Å Stokes  $V$  profile differs from the 8662 and 8542 Å lines. All three have a considerable amount of signal in the wings, but the Stokes  $V$  signal in the 498 Å line wing is almost as strong as in the lobes of the profile. Furthermore, the lobes of 8498 Å have self-reversal like structures which are not seen in the two other lines. These structures are caused by the magnetic field gradients in the atmosphere. The gradients decay with height, so that the 8498 Å line is formed in a region with a stronger gradient than the two other lines. If the magnetic field were instead constant with height the 8498 Å Stokes  $V$  profile would look very much like the 8662 and 8542 Å profiles.

The Stokes  $I$  profile amplitude and shape do not change as a function of horizontal position since we used the field-free approximation. In a weak magnetic field Stokes  $V$  should be roughly proportional to  $\frac{dI}{d\lambda}$ , though strict proportionality holds only in the absence of gradients. The field in the simulation is weak, and the large magnetic field gradients are in the photosphere, so it is not surprising that the shape of the Stokes  $V$  profiles does not change much in the horizontal direction. The only visible difference is the amount of Stokes  $V$  signal in the line wings. There is more signal in the line wings if the line is formed at the edges of the simulation domain than if it is formed in the middle of the domain. This is true for all three lines. The  $z$ -component of the magnetic field changes sign in the middle and so do the Stokes  $V$  profiles as well. The Stokes  $V$  amplitudes in the initial atmosphere as a function of horizontal position are shown in figure 5. They are largest at the sides of the domain where the field is entirely vertical. The 8498 and 8542 Å lines have roughly the same amplitudes even though they are formed at different heights. The effective Landè  $g$ -factors for the 8498, 8662, and 8542 Å lines are 1.07, 1.10, and 0.83 respectively, so it is

not surprising that the 8542 Å Stokes  $V$  signal has almost the same amplitude as the 8498 Å.

### 3.2. Time evolution of the Stokes profiles

Waves propagating through the formation regions of the lines cause oscillations in Stokes  $I$  and  $V$  amplitude as well as Stokes  $V$  amplitude and area asymmetries (figure 6). The Stokes  $I$  oscillation time series are quite similar in all three lines except for the slightly more saw tooth-like and less smooth appearance in 8662 and 8542 Å line time series. The large intensity peak visible in all three lines at about 800 seconds coincides with the smallest plasma- $\beta$  value in the simulations thus coinciding with a shock causing a larger than normal compression of plasma. In general an increase in intensity, i.e. less absorption, is associated with a decrease in Stokes  $V$  amplitude. This relationship is most clearly seen in the 8498 Å time series. Small variations barely visible in the 8498 Å Stokes  $V$  amplitude time series are prominent in the 8662 and 8542 Å lines. The overall shape of the asymmetry time series resembles the shape of the piston (figure 2), i.e. fluid velocity as a function of time. The growing amplitude of the propagating waves is manifested in the increased amplitude of the asymmetry oscillations: the asymmetry oscillation of the 8498 Å line has a much smaller amplitude because it is formed lower.

Figure 7 shows the time evolution of the atmospheric velocity and Ca lines as a steepening wave propagates through the atmosphere. At first (time 1070 s) the velocity in the region where the Ca lines are mostly formed is negative and has a small amplitude resulting in an absorption profile that is only slightly blue-shifted. The shift is visible in the intensity profiles, but not in Stokes  $V$ . This is because the shift is not yet large enough to affect the blue lobe in Stokes  $V$ . The 8498 Å line is affected by the upward propagating wave before the other two Ca lines (time 1080 s). The velocity in the Ca 8498 Å formation region grows and the absorption profile shifts even more to the blue so that now not only the Stokes  $I$  but also  $V$  is more asymmetric ( $I$  more than  $V$ ). Later in time (time 1090 s) the 8662 and 8542 Å intensity profiles also start to become more asymmetric as the wave propagates upward. Finally (time 1110 s), the velocity gradients are large enough to cause the blue lobes of the Stokes  $V$  profile in 8662 and 8542 Å disappear completely. The 8498 Å line is formed lower where the gradients are not yet large enough to cause the lobe to disappear. Before the next wave arrives, the velocity amplitude becomes very small and the blue lobes start to gradually reappear until the Stokes  $V$  profiles are again fairly symmetric (time 1140 s). The next wave brings a positive velocity that causes the absorption profile to shift toward red and eventually the red lobes of the 8662 and 8542 Å Stokes  $V$  signals disappear (time 1200

s). The lobes reappear once the velocity becomes again very small and the absorption profile is centered around the non-shifted line core (time 1230 s).

This pattern of disappearing and reappearing Stokes  $V$  lobes repeats itself throughout the simulation. When the atmosphere is close to rest, an amplitude peak associated with a symmetric profile occurs.

The amplitudes of the Stokes  $V$  asymmetries, both area and amplitude, are closely tied to the amplitudes of the velocity gradients present in the atmosphere. In figure 8 are plotted the asymmetries as functions of the atmospheric velocity gradient. The velocity gradient is defined as the difference between the velocity at two heights, 0.5 and 1.3 Mm. A negative gradient indicates a velocity that increases upward and vice versa. The correlation between the asymmetries and the velocity gradients is stronger in the 8662 and 8542 Å lines. If the velocity gradient was determined lower in the atmosphere there would be a stronger correlation in the case of the 8498 Å line. The way the velocity gradient is defined works well most of the time. But there are cases when the definition fails and gives rise to the outlier points in figure 8, where a small asymmetry is associated with a very large velocity gradient. These large velocity gradients are actually very localized and at a height of 1 Mm and above, i.e. above the line’s main formation region. The line in these cases is formed mostly in a region where the velocity profile is nearly flat and does not cause large asymmetries in the line. Area and amplitude asymmetries may prove to be good diagnostics for atmospheric velocity gradients.

Not surprisingly, there is a similar relationship between the area asymmetries and the center of gravities of the Stokes  $I$  profiles (fig. 9). There is much more scatter in the case of amplitude asymmetries and line center of gravities. The center of gravity for a profile is defined as:

$$cog = \frac{\int_{\lambda_0}^{\lambda_1} (I_c - I) \lambda d\lambda}{\int_{\lambda_0}^{\lambda_1} (I_c - I) d\lambda},$$

where  $I_c$  and  $I$  are the continuum and line intensities, respectively. The center of gravity is actually related to an average of the bulk velocity. In this simulation, the times of maximum velocity gradient are also the maximum excursions of the bulk velocity, which explains the good correlation between the center of gravity and profile asymmetry.

Histograms of the amplitude and area asymmetries (figure 10) are fairly symmetric. The three Ca lines have slightly more negative than positive asymmetries i.e. the Stokes  $V$  blue lobe has in general a larger amplitudes than the red lobe. In the amplitude asymmetry histograms of the 8662 and 8542 Å lines peculiar side lobes can be found. These lobes

are not seen in the 8498 Å line where the histograms decay steadily on both sides. The lobes correspond to the extremely asymmetric Stokes  $V$  profiles associated with shocks. The transition from a symmetric Stokes  $V$  profile to a strongly asymmetric profile takes less time than the symmetric and strongly asymmetric phases. This is seen in the histograms where there are fewer moderately asymmetric profiles than symmetric and strongly asymmetric profiles. The cores of the area asymmetry histograms (right-most panels of figure 10) for the three Ca lines are similar. However, the 8662 and 8542 Å histograms have wings that extend to approximately -0.4 and 0.4 whereas the 8498 Å area asymmetries are considerably smaller. The extended wings are caused by the strongly asymmetric profiles associated with shocks.

### 3.3. Discussion

Waves propagating through and forming shocks in the formation regions of the Ca lines cause a time-varying pattern in the Stokes  $V$  profiles. As the local fluid velocity changes with the changing phase of the propagating wave, the line absorption profile is shifted away from the line core. This combined with velocity gradients in the atmosphere leads to a repeated pattern of disappearing and reappearing lobes in the Stokes  $V$  profiles. In the simulation large asymmetries in the Stokes  $V$  profiles are commonly found. Since the 8662 and 8542 Å lines are formed higher up in the atmosphere, where the wave amplitudes are larger, the time varying pattern is stronger in them than in the 8498 Å line. Similar dynamic behavior of Stokes  $V$  profiles as in our simulation has been seen in a 2D MHD simulation of the photosphere by Steiner et al. (1998). They simulated photospheric convection and its interplay with flux sheets in the intergranular lanes. The effect of the swaying flux sheet and passing shocks was visible in both the shape and wavelength of the Stokes  $V$  profiles.

Earlier work (e.g. Sanchez Almeida et al. 2003; Ploner et al. 2001; Grossmann-Doerth et al. 2000; Steiner et al. 1998; Grossman-Doerth et al. 1989, 1988) addressing the formation of large asymmetries in Stokes  $V$  profiles in the photosphere found that variations along the line-of-sight and polarity reversals in the atmosphere are important in producing high asymmetries. In our simulation the photospheric iron line in the wing of the 8498 Å Ca line has very little asymmetry in it. Since the piston used in the simulation is homogeneous over the domain, asymmetries can not rise from line profiles being shifted relative to one another. Only the magnetic field and velocity gradients are able to produce asymmetries, but the wave amplitude in the photosphere is not large enough to make the iron line highly asymmetric. This is in accordance with previous work where gradients in velocity and magnetic field alone seldom produce large asymmetries in photospheric lines. The situation is somewhat different

for the chromospheric lines. Highly asymmetric and even single-lobed Stokes  $V$  profiles are a fairly common occurrence in the simulated Ca lines even though no polarity reversals take place in a single “pixel” and the line-of-sight is along the vertical axis. Unlike in the photosphere, a combination of a velocity gradient and a magnetic field gradient is enough to produce single-lobed Stokes  $V$  signals in the chromosphere. The strong dependence of the area and amplitude asymmetries on the velocity gradients shown in figure 8 was heuristically explained for the LTE case by Grossman-Doerth et al. (1989): the relation between the total change of Zeeman shift and line Doppler shift in the lines formation region governs the magnitude of the profile asymmetry. This relation has been seen in observations as well: for example, Balasubramaniam et al. (1997) found a clear correlation in the 6301 and 6302 Å iron line center-of-gravities and Stokes  $V$  amplitude asymmetries.

The strong similarity in the Stokes  $V$  profile shapes at a given time along the horizontal direction shows that in the high- $\beta$  regime the effect of chromospheric magnetic field gradients on the asymmetries is not as strong as the effect of the velocity gradients. If the magnetic field scale height is set to be 4.25 Mm instead of 0.85 Mm, so that the magnetic field gradient is larger higher up, there still is very little difference in profile shape along the x-axis. The velocity gradients clearly dominate the formation of the asymmetries in the simulation.

If the Ca lines are formed in a region where acoustic waves are important and the field is only moderately strong we would expect to see this pattern in observations as well. Stokes  $V$  asymmetries may prove to be a possible diagnostic for estimating velocity gradients in the lines’ formation regions for fairly quiet-Sun areas with moderate magnetic flux. Spatial resolution will be a serious issue in trying to observe dynamic behavior similar to the simulation. Because of limited spatial resolution, polarity reversals and magnetic field distributions within a pixel will easily smudge out the asymmetries in the Stokes  $V$  profiles and decrease the signal amplitude. The comparison of observations with the simulated profiles is therefore not likely to be straight-forward. It should still be possible to observe wave propagation in the Stokes  $V$  profiles of the Ca IR triplet lines though one should not necessarily expect to see asymmetries as extreme as in the simulations.

The next step is to test if this simple simulation is able to reproduce line profiles observed in the quiet Sun. In the future, we plan to use quiet Sun observations of the Ca IR triplet lines from the SPINOR instrument (Socas-Navarro et al. 2005). Another interesting question to pursue is how a stronger magnetic field would affect the atmospheric dynamics and consequently the line profiles and their time-dependent behavior. Since a 3D MHD code with full radiative transfer is not available, using a similar approach as here, i.e. combining a 2D MHD code with radiative cooling and the Stokes synthesis code, is an attractive alternative.

Understanding the formation of the Ca IR triplet lines in a dynamic atmosphere will hopefully lead to a better interpretation of observations and ultimately give us new insight into the dynamics of the magnetic quiet Sun.

We are grateful to J.M. Borrero for constructive comments on the manuscript.

## REFERENCES

- Arregui, I., Oliver, R., & Ballester, J.L. 2003, *A&A*, 402, 1129
- Aschwanden, M. J. 2004, *Physics of the Solar Corona*, Springer
- Balasubramaniam, K. S., Keil, S. L., & Tomczyk, S. 1997, *ApJ*, 482, 1065
- Beckers, J. M., & Schultz, R. B. 1972, *Solar Phys.*, 27, 61
- Bogdan, T. J., Hansteen, M. C. V, McMurry, A., Rosenthal, C. S., Johnson, M., Petty-Powell, S., Zita, E. J., Stein, R. F., McIntosh, S. W., & Nordlund, Å. 2003, *ApJ*, 599, 626
- Buchholz, B., Ulmsneider, P. , & Cuntz, M. 1998, *ApJ*, 494, 700
- Cargill, P. J., Spicer, D. S., & Zalesak, S. T. 1997, *ApJ*, 488, 854
- Carlsson, M., & Stein, R. 1992, *ApJ*, 397, L59
- Carlsson, M., & Stein, R. 1994, in *Chromospheric Dynamics* (Institute of Theoretical Astrophysics, Oslo)
- Carlsson, M., & Stein, R. 1995, *ApJ*, 440, L29
- Carlsson, M., & Stein, R. 1997, *ApJ*, 481, 500
- Carlsson, M., & Stein, R. 2002, in *ESA SP-508: From Solar Min to Max: Half a Solar Cycle with SOHO*
- DeForest, C. E., & Gurman, J. B. 1998. *ApJLetters* 501, L217-L220
- Fawzy, D., Rammacher, W., Ulmscheider, P., Musielak, Z. E., Stepien, K. 2002, *A&A*, 386, 971
- Fossum, A., & Carlsson, M. 2005, *Nature*, 435, 919



- De Groof, A., & Goossens, M. 2000, *A&A*, 356, 724
- De Groof, A., Paes, K., & Goossens, M. 2002, *A&A*, 386, 691
- Grossman-Doerth, U., Schüssler, M., & Solanki, S. K. 1988, *A&A*, 206, L37
- Grossman-Doerth, U., Schüssler, M., & Solanki, S. K. 1989, *A&A*, 221, 338
- Grossmann-Doerth, U., Schüssler, M., Sigwarth, M., & Steiner, O. 2000, *A&A*, 357, 351
- Gustafsson, B. 1973, *Uppsala Astr.Obs.Ann.* 5, No. 6
- Huang, P., Musielak, Z. E., & Ulmschneider, P. 1999, *A&A*, 342, 300
- Judge, P., Casini, R., Tomczyk, S., Edwards, D. P., & Francis, E. 2001, in *Coronal Magnetometry: a feasibility study* (NCAR/TN-446-STR)
- Judge, P., Carlsson, M., & Stein R. 2003, *ApJ*, 597, 1158
- Kliem, B., Dammasch, I. E., Curdt, W., & Wilhelm, K. 2002, *ApJLetters*, 568, L61-L65.
- Kunasz, P., & Auer, L. H. 1988, *J.Quant.Spectrosc.Radiat.Transfer*, 39,67
- Landolfi, M., & Landi degl’Innocenti, E., 1996, *Solar Phys.*, 164, 191
- Lites, B. W. 2002, *ApJ*, 573, 431
- Manso Sainz, R., & Trujillo Bueno, J. 2003, *Phys. Review Letters*, 91, 111102
- Martínéz Píllet, V., Lites, B. W., & Skumanich, A. 1997, *ApJ*, 474, 810
- McIntosh, S. W., Fleck, B., & Judge, P. G. 2003, *A&A*, 405, 769
- Mckenzie, J. F., & Axford, W. I. 2000, *Solar Phys.*, 193, 153
- Mein, P., & Rayrole, J. 1985, *Vistas Astron.* 28, 567
- Nakariakov, V. M. 2003, in *Dynamic Sun*, Cambridge University Press, 314-334
- Ofman L., Romoli, M., Poletto, G., Noci, G., & Kohl, J.L. 1997, *ApJLetters*, 491, L111-L114
- Ofman, L., Nakariakov, V. M., & DeForest, C. E. 1999, *ApJ*, 514, 441-447.
- Ofman, L., Nakariakov, V. M., & Sehgal, N. 2000, *ApJ*, 533, 1071
- Ploner, S. R. O., Schüssler, M., Solanki, S. K., Sheminova, V. A., Gadun, A. S., & Frutiger, C. 2001, in *ASP Conf. Proceedings*, 236, *Solar Polarization Workshop 3*

- Rammacher, W., & Cuntz, M. 2003, *ApJL*, 594, L51
- Rayrole, J., & Mein, P. 1993, in *ASP Conf. Ser. 46:IAU Colloq.* 141, 170
- Rees, D. E. 1969, *Solar Phys.*, 10, 268
- Sanchez Almeida, J., & Lites, B. W. 1992, *ApJ*, 398, 359
- Sanchez Almeida, J., Emonet, T., & Cattaneo, F. 2003, *ApJ*, 585, 536
- Shchukina, N., & Trujillo Bueno, J. 2003, in *ASP Conf. Ser. 307, Solar Polarization Workshop*  
3
- Sigwarth, M. 2001, *ApJ*, 563, 1031
- Skartlien, R., Stein, R. F., & Nordlund, Å. 2000, *ApJ*, 541, 468
- Socas-Navarro, H., Trujillo Bueno, J., & Ruiz Cobo, B. 2000, *ApJ*, 530, 977
- Socas-Navarro, H., Trujillo Bueno, J., & Ruiz Cobo, B. 2001, *ApJ*, 550, 1102
- Socas-Navarro, H., Elmore, D., Tomczyk, S., Pietarila, A., Darnell, A., Lites, B., & Hegwer, S. (2005), *Solar Phys.*, in press
- Steiner, O., Grossmann-Doerth, U., Knölker, M., & Schüssler, M. 1998, *ApJ*, 495, 468
- Thompson, B. J., Plunkett, S. P., Gurman, J. B., Newmark, J. S., St Cyr, O. C., & Michels, D. J. 1998, *Geophys. Res. Lett.*, 25, 2465-2468
- Tirry, W. J., & Berghmans, D. 1997, *A&A*, 325, 329
- Tsiklauri, D., Nakariakov, V. M., & Rowlands, G. 2003, *A&A*, 338, 311
- Tziotziou, K., Tsiropoula, G., & Mein, P. 2002, *A&A*, 381, 279
- Wahlstrom, C., & Carlsson, M. 1994, *ApJ*, 433, 417
- Wang, T. J., Solanki, S. K., Curdt, W., Innes, D. E., & Dammasch, I. E. 2002, *ApJ*, 574, L101-L104.
- Wittmann, A. 1974, *Solar Phys.*, 35, 11W
- Ziegler, U., & Ulmschneider, P. 1997, *A&A*, 324, 417

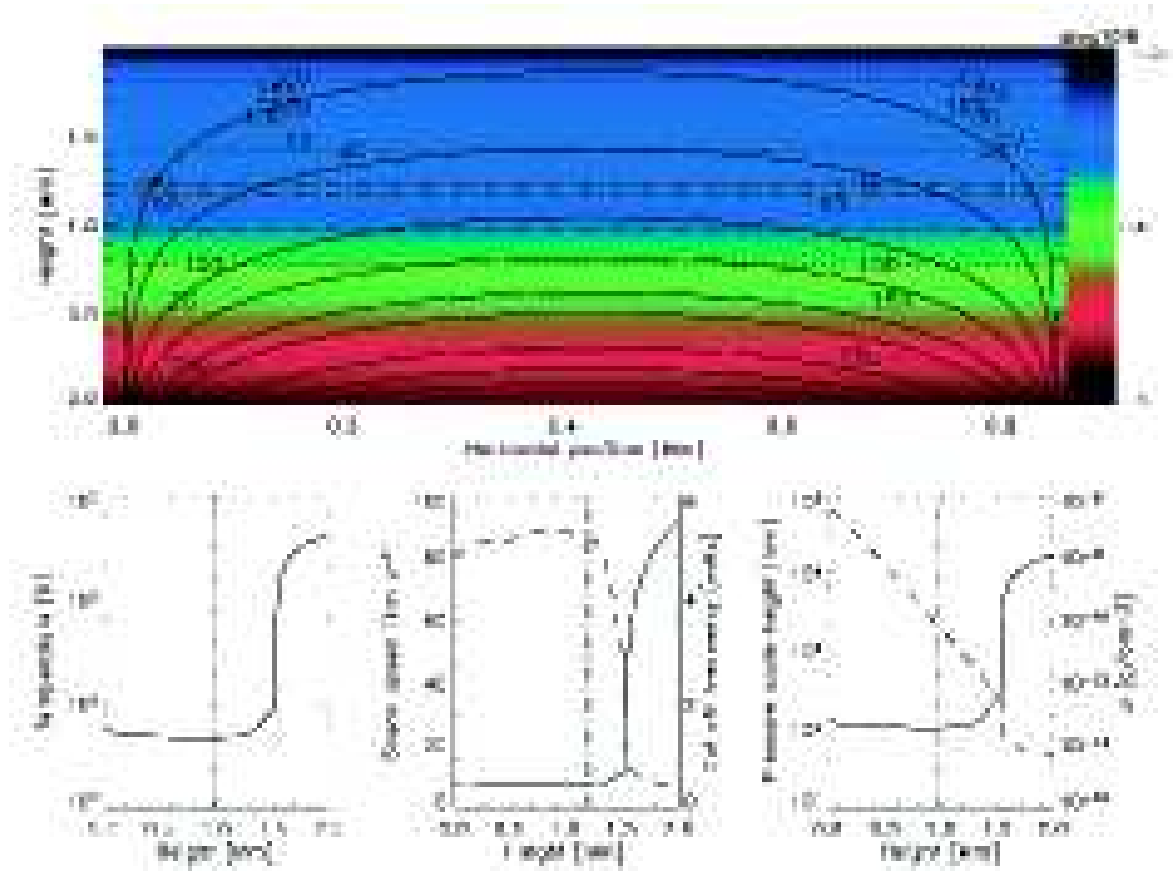


Fig. 1.— The initial atmosphere. Upper panel shows the initial magnetic field configuration. The color scale indicates field strength on a logarithmic scale. Solid lines are representative magnetic field lines. Dotted lines are plasma- $\beta$  contours. Dash-dotted lines are the heights where optical depths in the Ca line cores equal unity. The lower panels show the temperature (left panel), sound speed and acoustic cut off frequency (center panel, the left ordinate is for the solid line and right ordinate for the dashed line), pressure scale height and density (right panel) as functions of height.

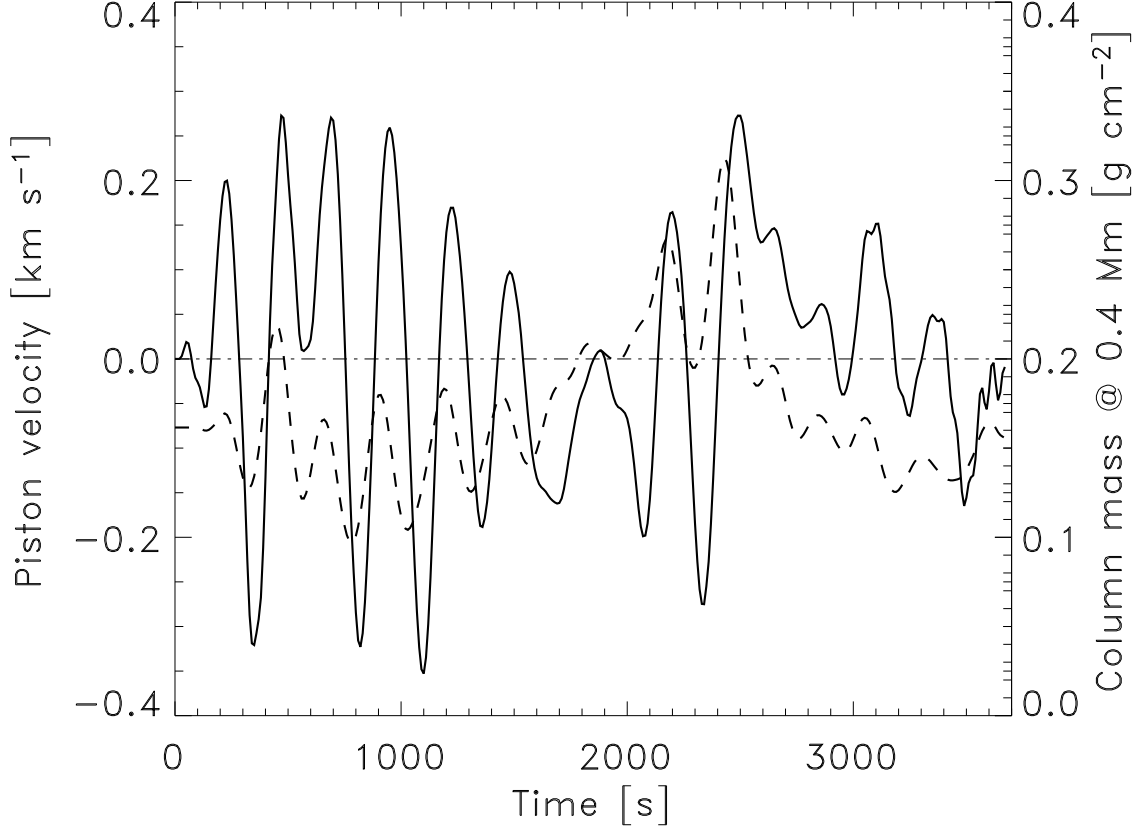


Fig. 2.— The piston velocity at the lower boundary as a function of time. Negative and positive velocities indicate upward and downward motion, respectively. Note the asymmetry of the piston in the first half of the simulation with positive velocities dominating. The column mass at a fixed height, 0.4 Mm is also shown (dashed line, left ordinate).

Table 1. Spectral lines.

	Level	$E_i$	$E_k$	$\log gf$	$Z(0)$	$\min(Z)$	$\max(Z)$	$\text{mean}(Z)$
	Configuration	[ $\text{cm}^{-1}$ ]	[ $\text{cm}^{-1}$ ]		[Mm]	[Mm]	[Mm]	[Mm]
Ca II 8542 Å	$^2P_{3/2}^O - ^2D_{5/2}$	13711	25414	-0.36	1.24	0.89	1.43	1.19
Ca II 8662 Å	$^2P_{1/2}^O - ^2D_{3/2}$	13650	25192	-0.62	1.16	0.87	1.36	1.15
Ca II 8498 Å	$^2P_{3/2}^O - ^2D_{3/2}$	13650	25414	-1.32	0.97	0.80	1.17	1.02
Fe I 8497 Å	$^3F_3 - ^3F_2$	37024	48797	-0.95				

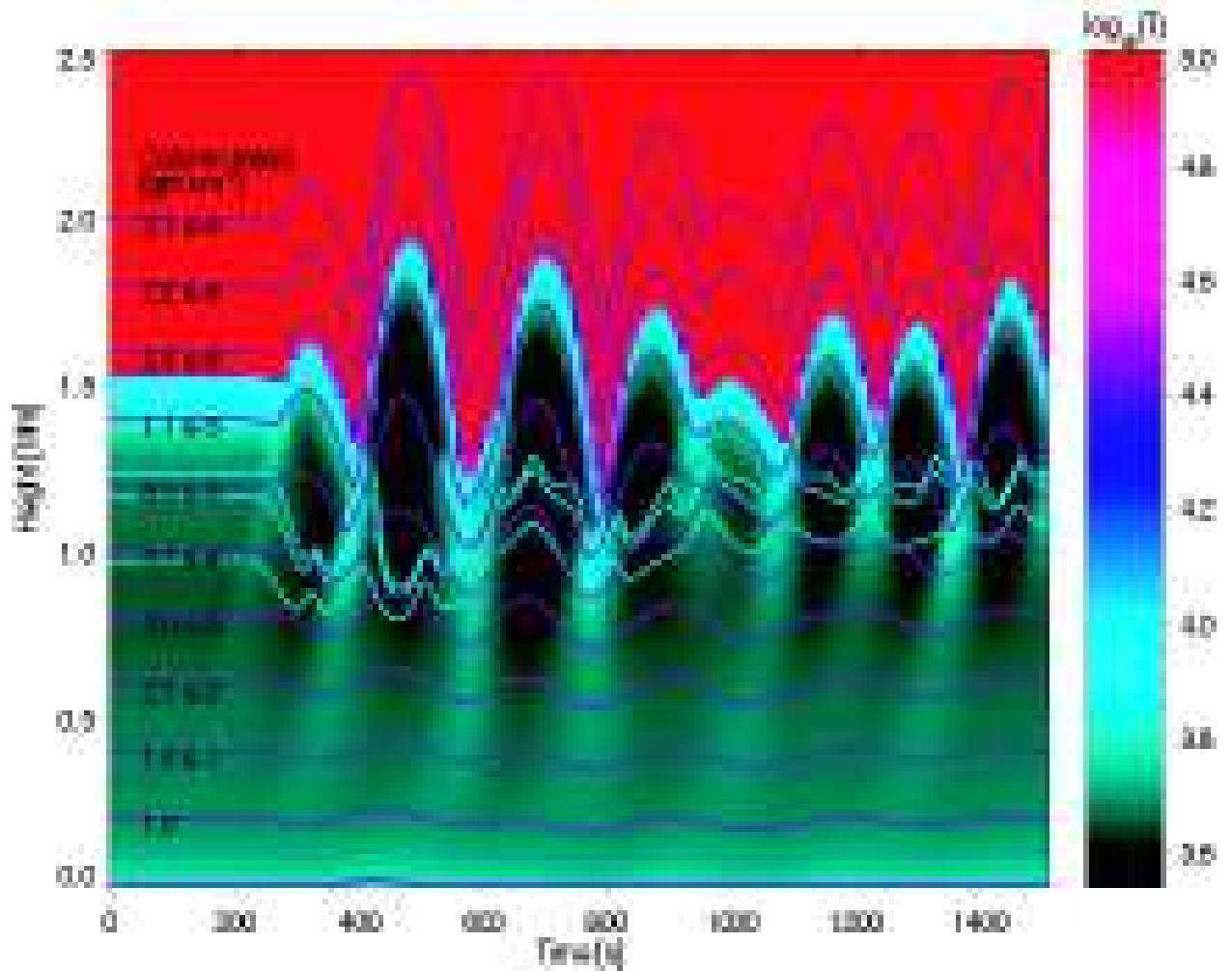


Fig. 3.— The dynamic evolution of the first 1500 seconds in the radiation hydrodynamic simulation. The color scale of the image shows the temperature as a function of height (y-axis) and time (x-axis). Over-plotted in turquoise are the formation heights ( $\tau_\nu = 1$  at line core) of the Ca IR triplet lines (lowest line: 8498 Å, middle:8662 Å, top:8542 Å) and in blue the locations of fixed column masses. The steepening of the waves into shocks as they propagate upward in the atmosphere is clearly seen in all three.

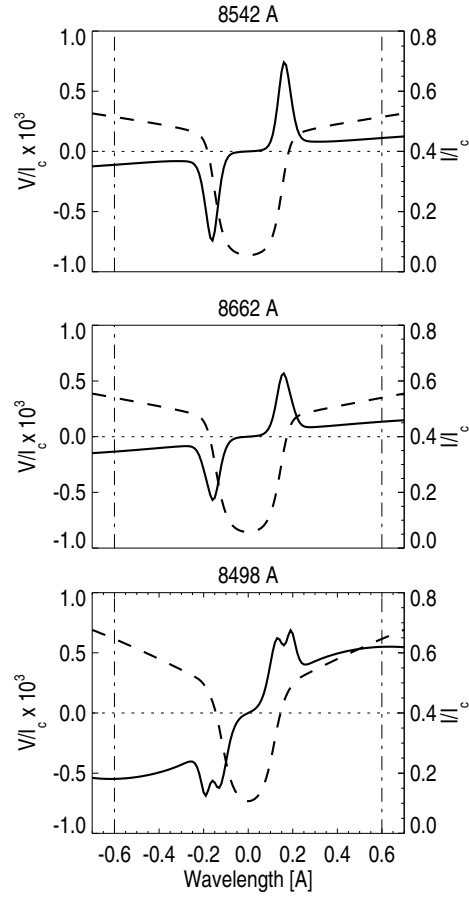


Fig. 4.— Stokes  $I$  and  $V$  profiles for the Ca lines in the initial atmosphere. In all three panels the left ordinate shows the scale for the solid line (Stokes  $V$ ) and the right ordinate for the dashed line (Stokes  $I$ ). Both Stokes  $I$  and  $V$  are referred to the quiet Sun continuum. The vertical dash-dotted lines show the integration range used in defining the area asymmetry.

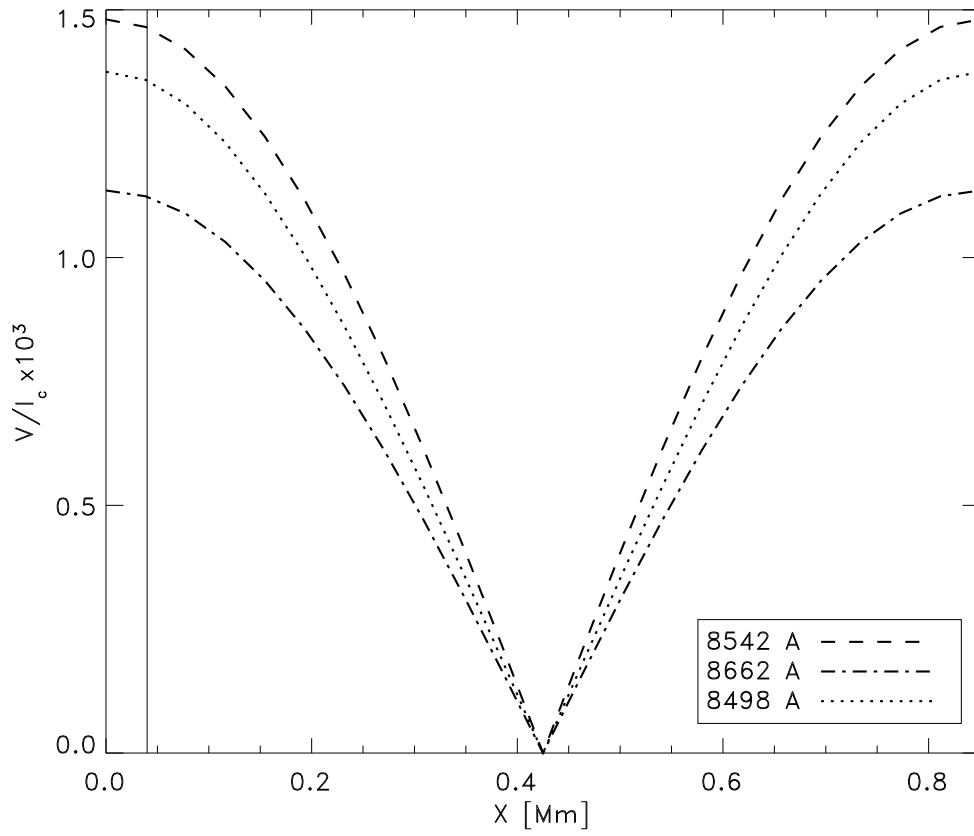


Fig. 5.— Stokes  $V$  amplitude as a function of horizontal position in the initial atmosphere. The Stokes  $V$  amplitudes are referred to the continuum intensity. The vertical line shows the position where the individual profiles shown in the paper are from.

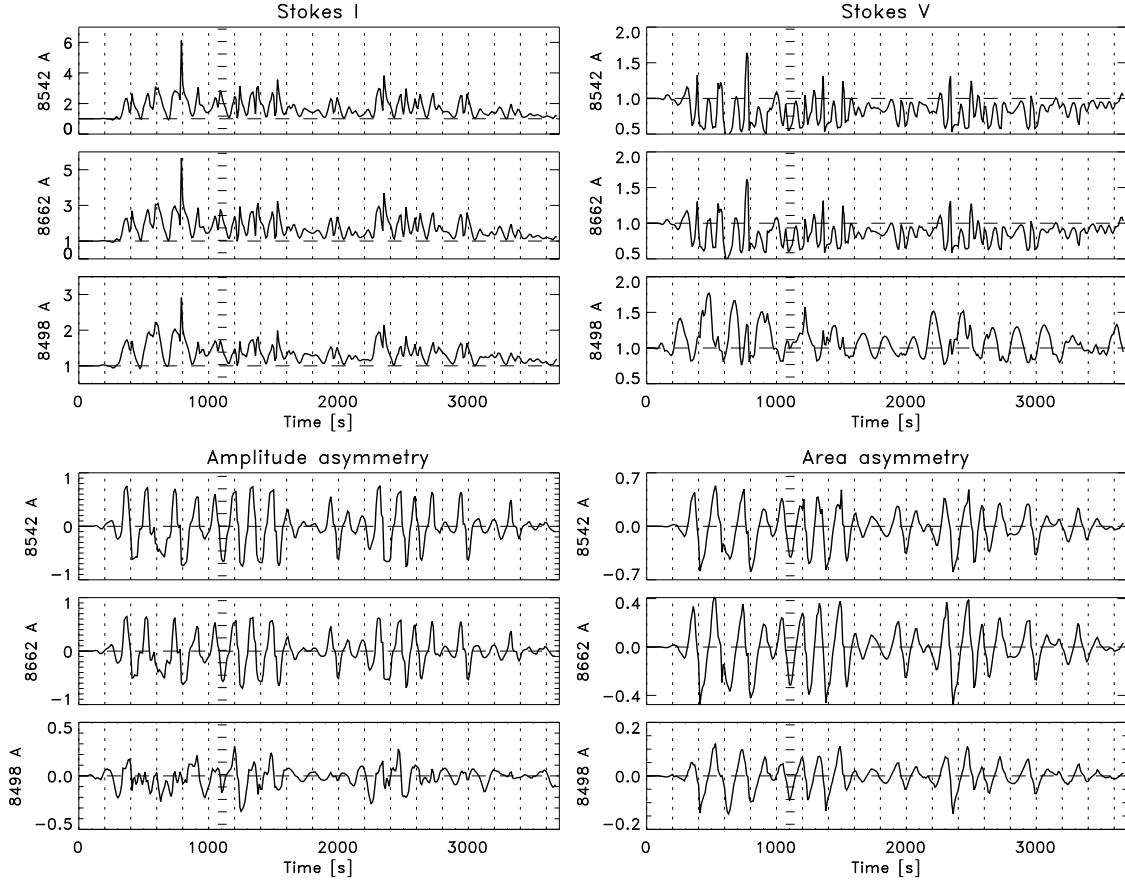


Fig. 6.— Time evolution of Stokes  $I/I(t=0)$  (measured at line core) and Stokes  $V/V(t=0)$  amplitude, Stokes  $V$  area and amplitude asymmetries at the left edge of the simulation domain. The vertical dashed lines are located at every 20 seconds interval. The region of horizontal lines shows the location of the shock discussed in detail in the text.



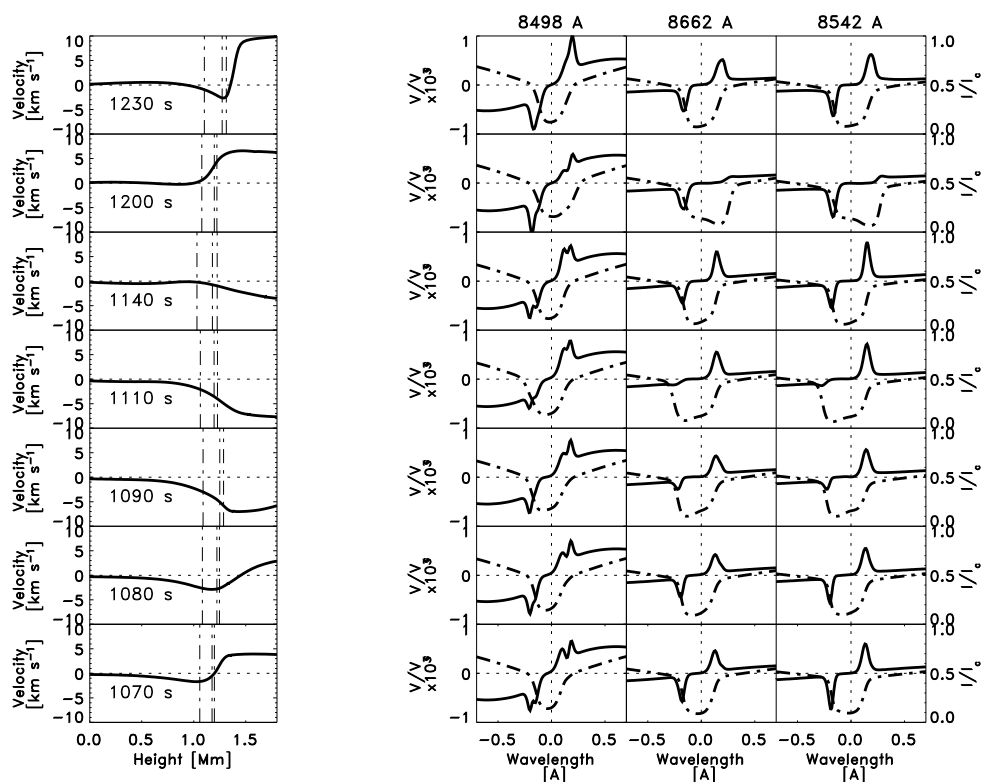


Fig. 7.— Time evolution of a shock. Each row in the figure represents a snapshot of the simulation. The time for the snapshot is shown in the upper part of the first panel of each row. Shown are the velocity in the atmosphere as a function of height and the Stokes  $V$  (left ordinate, solid line) and Stokes  $I$  (right ordinate, dash-dotted line) profiles for the three Ca lines. The dashed lines in the velocity panels show the height where the Ca line center optical depths equal unity.

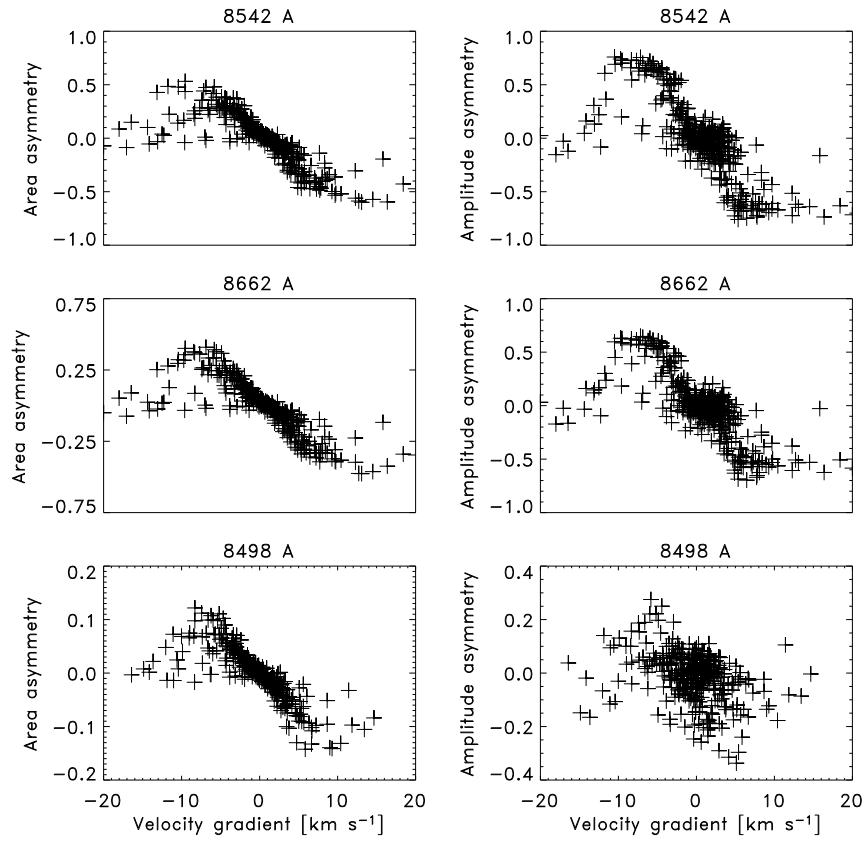


Fig. 8.— Amplitude and area asymmetries as a function of the velocity gradient. The gradient is determined in the upper photosphere/chromosphere, 0.5-1.3 Mm.

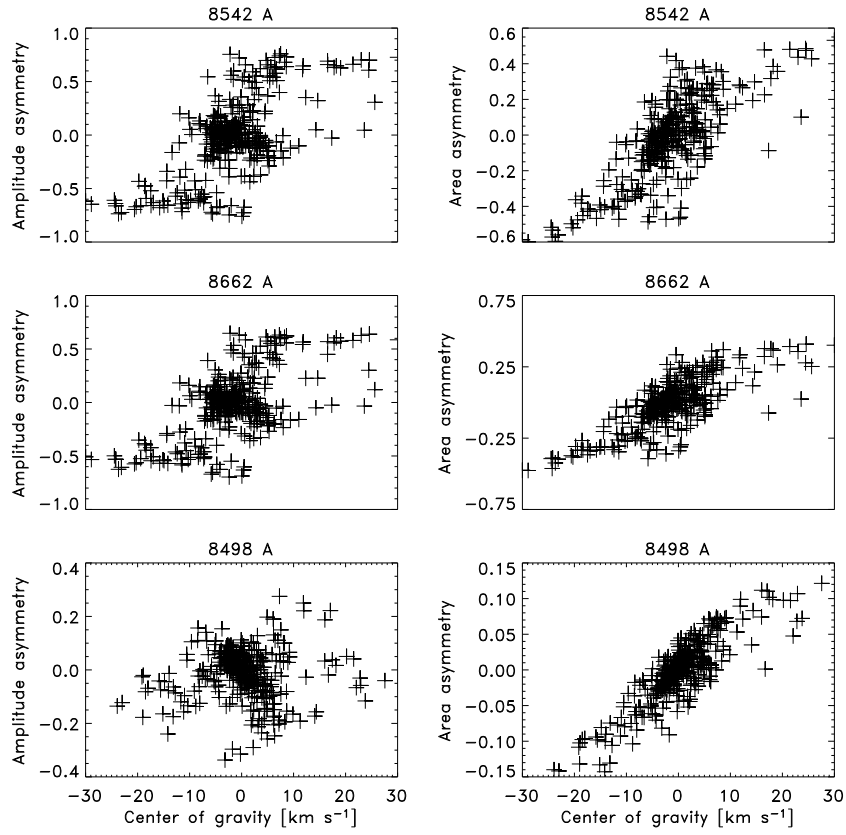


Fig. 9.— Amplitude and area asymmetries as a function of the center of gravity for the Ca lines.

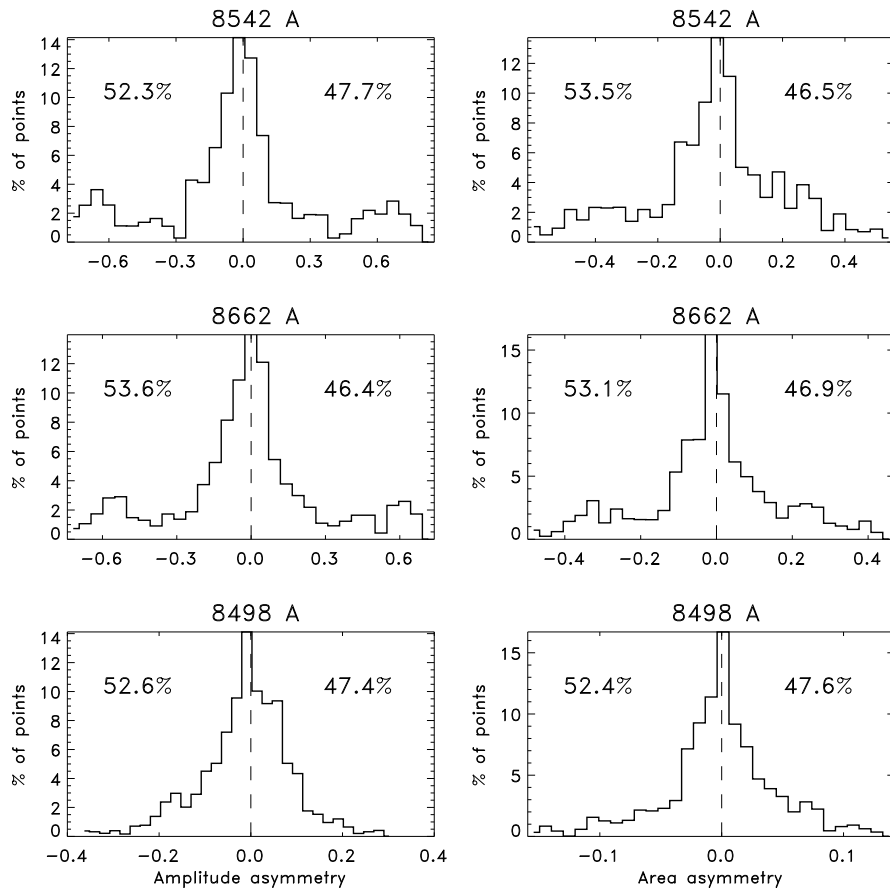


Fig. 10.— Histograms of amplitude and area asymmetries in the Ca lines. The percentages show the amount of negative and positive asymmetries.